Title

3D/4D Reconstruction and Quantitative Total Body Imaging

Journal

PET Clinics, 16(1)

ISSN

1556-8598

Authors

Qi, Jinyi
Matej, Samuel
Wang, Guobao
et al.

Publication Date

2021

DOI

10.1016/j.cpet.2020.09.008

Peer reviewed

HHS Public Access

Author manuscript

PET Clin. Author manuscript; available in PMC 2022 January 01.

Published in final edited form as:

PET Clin. 2021 January ; 16(1): 41–54. doi:10.1016/j.cpet.2020.09.008.

3D/4D reconstruction and quantitative total body imaging

Jinyi Qi[*,1], **Samuel Matej**[*,2], **Guobao Wang**[*,3], **Xuezhu Zhang**[1]

[1]Department of Biomedical Engineering, University of California, Davis, CA, USA

[2]Department of Radiology, University of Pennsylvania, Philadelphia, PA, USA

[3]Department of Radiology, University of California Davis Medical Center, Sacramento, CA, USA

Synopsis

This chapter describes methods for image formation from raw measurements in total-body PET. Challenges and opportunities in total-body PET image reconstruction are discussed.

Keywords

PET reconstruction; direct parametric reconstruction; time of flight; long axial FOV; kernel reconstruction; data corrections

1. Introduction

Image reconstruction takes the measured coincidence events as the input and estimates the spatial and temporal distribution of the radioactive tracers within the scanned object. Total-body PET image reconstruction follows a similar procedure to the image reconstruction process for standard whole-body PET scanners. Both analytical and iterative reconstruction methods can be applied. Special considerations need to be taken for the extended axial field of view (AFOV) and large amount of data. Some issues related to the long AFOV include the axial point spread function (PSF) and estimation of correction factors, such as detector normalization factors and those for scattered coincidence events. The large amount of data also requires attention with respect to the computational efficiency of reconstruction algorithms. One unique aspect of total-body imaging is the simultaneous coverage of the entire human body, which makes it very convenient to perform total-body dynamic PET scans. Therefore, 4D dynamic PET reconstruction and parametric imaging are of great interest in total-body imaging. This chapter covers some basics of PET image reconstruction and then focuses on 3D and 4D PET reconstruction for total-body imaging.

2. List-mode 3D image reconstruction

2.1 Basics

Total-body PET scanners have a huge number of lines of response (LORs). For example, the uEXPLORER scanner (United Imaging Healthcare, Shanghai, China) has more than half a

*Equal contributions

million individual crystals, forming over 90 billion LORs [1,2]. With time-of-flight (TOF) information, the number of elements in a TOF sinogram can be more than one trillion, which is far greater than the number of coincidence events that could be detected in a regular scan. For example, a one-hour dynamic scan following a 256 MBq ^{18}F-FDG injection acquired 61 billion prompt (true + scattered + random) coincidences [2]. Therefore, list-mode based iterative reconstruction is a natural choice to avoid handling large sinograms.

The data model for total-body image reconstruction is the same as that derived for standard PET image reconstruction[3–5]. The expectation of the i^{th} LOR measurement is related to the radioactivity distribution image $\boldsymbol{x} \in R^{N_v \times 1}$ by

$$\bar{y}_i = (\boldsymbol{P}\boldsymbol{x} + \boldsymbol{s} + \boldsymbol{r})_i$$

where $\boldsymbol{P} \in R^{N_l \times N_v}$ is the system matrix with the $(i, j)^{th}$ element representing the probability of detecting an event originated from the j^{th} voxel in the i^{th} LOR, $\boldsymbol{s} \in R^{N_l \times 1}$ and $\boldsymbol{r} \in R^{N_l \times 1}$ denote the expectation of the scattered and random coincidences, respectively [6]. N_v and N_l are the total numbers of voxels and LORs, respectively. The list-mode log likelihood function can be written as

$$L(\boldsymbol{x}) = \sum_{k=1}^{N_k} \ln(\boldsymbol{P}\boldsymbol{x} + \boldsymbol{s} + \boldsymbol{r})_{i_k} - \sum_{j=1}^{N_v} \epsilon_j x_j$$

$$\epsilon_j = \sum_{i=1}^{N_l} P_{ij}$$

where N_k is the total number of list-mode events, i_k is the LOR index of the k^{th} event, and ϵ_j is the overall efficiency of detecting events from the j^{th} voxel[3].

The maximum likelihood (ML) estimation can be obtained by the ML expectation maximization (EM) algorithm [3]

$$\hat{x}_j^{n+1} = \frac{\hat{x}_j^n}{\epsilon_j} \sum_{k=1}^{N_k} \frac{P_{i_k j}}{(\boldsymbol{P}\boldsymbol{x} + \boldsymbol{s} + \boldsymbol{r})_{i_k}}$$

with x^0 starting from a uniform image.

One of the key components in iterative image reconstruction is the system matrix $\boldsymbol{P}$. By using a more accurate data-generation model than ideal line integrals used in the filtered backprojection reconstruction method, iterative methods can improve both the spatial resolution and the noise properties of reconstructed images. At the same time, however, an accurate model also means higher computation cost and prolonged image reconstruction

time. To address this challenge, a factored system matrix is often used [7,8]. While a complete factored model includes blurring components in both image and sinogram domains [9], list-mode reconstruction often uses an image domain resolution model [10], where the system matrix $\boldsymbol{P}$ is factored into

$$\boldsymbol{P} = \boldsymbol{NAGR}$$

where $\boldsymbol{N}$ and $\boldsymbol{A}$ are diagonal matrices containing the normalization factors and object attenuation factors, respectively, for each LOR, $\boldsymbol{G}$ is the geometric projection matrix that is calculated by a ray-tracing algorithm with a TOF kernel, and $\boldsymbol{R}$ is a point spread function (PSF) matrix that models the resolution degradation effects, such as the positron range, photon acollinearity, and detector responses including inter-crystal penetration and inter-crystal scatter effects.

Many components in the above model can be estimated in the same way as for standard PET reconstruction. For example, attenuation factors are estimated using a co-registered CT scan with bi-linear transformation [11,12]. Random coincidences can be estimated using either a delayed window technique or based on singles rates [13–15]. However, other components require special considerations for total-body image reconstruction. In the following sections, we will discuss a few unique aspects in the total-body reconstruction with a long AFOV scanner.

2.2 Point spread function modeling

The major component in the PSF model is the parallax error caused by annihilation photon crystal penetration. In a standard clinical PET scanner with ~20-cm AFOV, the parallax error mostly occurs in the radial direction. For a long AFOV scanner, the parallax error also occurs in the axial direction for the LORs formed between crystals with a large ring difference. As illustrated in Figure 1, a more oblique LOR (red color) penetrates more adjacent crystals than a less oblique LOR (blue color). Using the uEXPLORER scanner as an example, the axial width of a direct LOR with ring difference of zero is 2.85 mm, which is equal to the crystal pitch, whereas the axial width of an oblique LOR formed by two crystals 180 degree apart transversely with a polar angle of 57 degree (the maximum acceptance angle) is 27.6 mm, almost 10 times of that of a direct LOR. Such axial parallax error is not noticeable in standard clinical PET scanner with a 20-cm AFOV. As a result, the point spread function in long AFOV scanner is dependent on both the radial and axial positions.[16]

To model the spatially variant PSF, point source reconstructions can be used. Point source projections are either simulated [17] or measured [7,8] at different radial and axial positions and the data are reconstructed to obtain the PSF models. Figure 2 shows reconstructions of a set of simulated point sources inside a simulated 2-m long scanner [17] at different axial positions on the center axis of the scanner. Clearly, we can observe the degradation in the axial resolution as the point source moves from the axial boundary to the axial center. The resolution degradation effect is less dramatic than the change of the axial width of oblique LORs because the effect of oblique LORs is mitigated by direct LORs passing through the

same point. The major effect of the parallax error is still in the radial direction. Figure 3 shows the transaxial profile of a reconstructed point source at 17.2 cm radial offset. Radial elongation is apparent even at this modest radial offset. The FWHM (Full Width at Half Maximum) and FWTM (Full Width at Tenth Maximum) values of the point spread function at selected radial locations are listed in Table 1 for comparison. (See also Figure 10 in Section 3.4.)

2.3 Normalization

Normalization is used in reconstruction to compensate for the variations in detector efficiencies and hardware related interference patterns [18]. It can also include any geometric factors that are not modeled in the system matrix $\boldsymbol{P}$. Normalization factors are computed by comparing measured projections of a physical phantom with known activity distribution and the prediction using the system model. Due to simplifications in the calculation of the system matrix, normalization is often required even for simulated PET scanners with uniform detector response [17]. Figure 4 shows a sinogram of a simulated uniform cylinder in a total-body scanner. While the simulated detectors have uniform response, we can clearly observe pronounced block patterns, which are caused by the combination of inter-crystal scatters and the energy weighted centroid positioning algorithm used in the Monte Carlo simulation. The energy weighted centroid effectively shifts detected events away from the edge crystals inside a detector block and hence reduces the apparent detection efficiency of edge crystals. In simulations, a number of geometric symmetries can be used to reduce the noise in the normalization sinogram so that a direct normalization based on the ratio between the measurement and prediction in each LOR can be used [17]. For a real scanner, direct normalization can be noisy, so component-based normalization is often preferred to decompose the normalization factors into several components with fewer number of unknowns. The parameters can be estimated using either direct calculation [18] or maximum likelihood estimation[19].

Regardless whether direct normalization or component-based normalization is used, we need sufficient true coincidence events in each sinogram for normalization factor estimation. In a long AFOV scanner, oblique LORs with a large ring difference have low efficiency in detecting true coincidences due to reduced solid angle and high attenuation of the phantom. As a result, both scatter fraction and random fraction increase with increasing oblique angle of the LOR. The combination of these effects makes it very difficult to accurately estimate the normalization factors for LORs with extremely large ring differences. Therefore, to avoid noise propagation from the normalization factors into reconstructed images, it is beneficial to exclude the LORs with very large oblique angles in the reconstruction, even though this means we are not using all detected events. This practical limitation on the maximum acceptance angle is separate from the NECR calculation[20] or hardware limitations [1].

2.4 Scatter estimation and correction

In total-body imaging with a long axial FOV scanner, photons can have longer paths through the object, resulting in greater chance for multiple-scattering events than that in conventional PET scanners. While the single scatter simulation (SSS) or its variant can still be used to

estimate the scatter mean [21], Monte Carlo simulation can model multiple scatters more accurately. The major challenge in Monte Carlo based scatter estimation is the high computation cost. One way to reduce the simulation time is to compute the scatter sinogram on the detector block level by assuming that the scatter sinogram is relatively smooth after correction for detector efficiencies [17]. Another approach is to use parallel computation with GPU acceleration. An example of the scatter mean sinogram estimated by the Monte Carlo simulation of an XCAT phantom is shown in Figure 5. Apart from the block boundary effects, the scatter sinograms are fairly smooth in all selected TOF bins.

3. Efficient reconstruction using DIRECT framework (Direct Image Reconstruction for TOF data)

While list-mode reconstruction has the advantage of facilitating straightforward and accurate modeling (in forward projection) for each acquired event, this is at the cost of having to separately calculate forward and back-projection operations for each individual event, leading to high computational demands. DIRECT[22] represents an alternative, very efficient, reconstruction approach taking advantage of the considerably decreased angular sampling requirement for TOF data. This allows a dramatic decrease in the number of views compared to the classical TOF-sinogram data and thus the ability to process many events together. It also permits the utilization of image-like partitioning of the TOF data into histo-images, which in turn allows very efficient and highly parallelizable reconstruction operations. Although both uExplorer[1] and PennPET Explorer[21] scanners use list-mode reconstruction as their default tool providing practical reconstruction times, high computational efficiency of DIRECT reconstruction approach will be especially beneficial for 3D/4D studies using wide acceptance angles and many dynamic or temporal frames.

3.1 DIRECT data partitioning

The DIRECT framework is based on two key steps: the acquired list-mode events are first sorted into a relatively small set of (transverse and co-polar) angular “views” according to the TOF angular sampling requirements [23,24] and then they are histogrammed into a set of “histo-images” (one histo-image per view; see Figure 6). Traditionally, binned TOF events are histogrammed into TOF-sinograms or “histo-projections,” which are projections extended in the TOF direction (with their sampling intervals relating to the projection geometry and TOF resolution). Although the histo-projections use also only a limited number of views similarly to DIRECT, the histo-projection data are in a different geometry/space from the reconstructed images. On the other hand, in the DIRECT approach the acquired events are histogrammed directly to the “most-likely” voxels of the histo-images. Histo-images are defined by the geometry and desired resolution units - reconstructed image voxels of the desired size. Acquired events and all correction factors are directly placed into the voxels of their respective histo-images, which have a one-to-one correspondence with the reconstructed image voxels, which allows efficient implementation of data correction and reconstruction operations, without the need of any ray-tracing or interpolations within the forward/back-projections.

3.2 Forward- and back-projection operations in DIRECT framework

Modeling of the acquired data (forward-projection) within the histo-image format can be simply implemented via a 3D convolution-like operation applied to the current estimate of the image using a specific kernel for each view. Each kernel has an ellipsoidal shape elongated along the view direction, as given by the TOF, detector (LOR), and other resolution effects. Back-projection is simply the transpose of forward-projection. For spatially invariant detector resolution kernels, very fast forward/back-projection operations can be implemented within DIRECT using Fourier-based approaches [22]. For spatially variant and asymmetric kernels, a parallel implementation of the forward- and back-projection operations can be efficiently implemented on a graphical processing unit (GPU) with comparable speeds for practical kernel and image sizes to the Fourier-based implementation with invariant kernels [25]. Correction data (attenuation and normalization factors, and scatter and randoms estimates) are efficiently generated directly in the histo-image geometry [22,26]. Attenuation and sensitivity factors, including gap effects (between detector modules) can be accurately and efficiently calculated using Fourier-based approaches [27].

3.3 DIRECT framework reconstruction

In the classical sinogram-based or histo-projection-based reconstruction approaches the reconstruction operations need to operate between data and image spaces with different geometries, requiring tracing and interpolation operations between the two spaces or different spectral grids in Fourier-based approaches, affecting both speed and accuracy of the reconstruction operations. On the other hand, in DIRECT approach all operations are voxel-wise multiplications or additions on/between two image structures with the same geometries, without the need of any spatial or spectral interpolations.

In *statistical iterative reconstruction algorithms*, the corrections, which are generated in the histoimage format, are applied (added or multiplied in) during the forward projection operation, and both the discrepancy and update operations of the algorithm are performed on the image structures. An additional advantage is that the attenuation factors can be easily and more accurately applied here before the forward projection and detector blurring operations, thus avoiding an approximation often done in conjunction with the image-based resolution modeling where the attenuation factors are usually applied only after the blurring (and geometric projection) operations. Iterative-DIRECT was shown to provide comparable quality and contrast-vs.-noise curves to the list-mode reconstruction for matched resolution models, but with substantially - an order of magnitude - shorter reconstruction times (see Figures 7 and 8) [26].

In the *analytic algorithm* the reconstruction operations are performed again very efficiently on the consistent spatial (or spectral) image structures. The analytic reconstruction filter takes into account also the data resolution models (in addition to the TOF resolution). For the analytic algorithm data have to be pre-corrected before the reconstruction for all of the data imperfections (normalization sensitivity, attenuation, scatter, randoms, dead-time). Gaps in the data inbetween the detector modules create decreased values in the histo-images, which are however non-zero (due to the view grouping), and can be therefore

straightforwardly corrected by the correspondingly generated geometric sensitivity. On the other hand, missing regions in the oblique data (due to the finite detector extent) need to be estimated from the available data, for example, by reprojection of a first-pass reconstruction from the complete non-oblique data, as in the 3D-RP and 3D-FRP reprojection algorithms [28,29]. For typical clinical data (with typical number of acquired prompts) analytic-DIRECT has been shown to provide similar contrast performance to iterative-DIRECT when applying the same resolution models [30].

3.4 Special considerations for long axial FOV data

Similar to the list-mode reconstruction, there are important considerations to be taken into account in DIRECT reconstruction due to the large increase of the axial acceptance angle. For example, many practical approximations related to the oblique data (such as axial binning/mashing, scatter estimations, etc.) have to be revisited and carefully treated. Additionally, there is a large variation in the sensitivity and attenuation factors as function of the oblique angles (with up to an order of magnitude changes) and large variation of the axial resolution. Combination of such data without proper modeling will create inconsistencies in the reconstruction model and will also affect the convergence rates.

An example of the variations of the counts (i.e., sensitivity) in the data with and without attenuation as a function of the oblique angle is shown in Figure 9. Figure 10 illustrates variations of the axial PSF resolution in the data space (as a function of the oblique angle) and in the reconstructed image (as a function of the axial acceptance angle) in iterative-DIRECT reconstruction without and with modeling of the axially varying resolution.

4. 4D reconstruction for total-body dynamic PET

4.1 Frame-by-frame reconstruction using the kernel method

In the setting of dynamic PET imaging, the expectation of the i^{th} LOR measurement in the m^{th} time frame is described by

$$\bar{y}_{i,m} = \left(\boldsymbol{P}\boldsymbol{x}_m + \boldsymbol{s}_m + \boldsymbol{r}_m\right)_i$$

for $m = 1, \ldots, N_m$ with N_m the total number of time frames[1]. Similar to the kernel method for standard dynamic PET image reconstruction [31-33], we can use a kernel representation to describe the tracer activity in the j^{th} voxel in the m^{th} frame of a total-body dynamic scan,

$$x_{j,m} = \left(\boldsymbol{K}\boldsymbol{\alpha}_m\right)_j$$

where $\boldsymbol{K}$ is the sparse kernel matrix built from the image prior and $\boldsymbol{\alpha}$ is the unknown kernel coefficient image.

[1]Here in the forward projection model, a frame-independent system matrix $\boldsymbol{P}$ is used for conceptual simplicity. In practice, frame-dependent $\boldsymbol{P}_m$ can be used to account for time-dependent factors when appropriate, such as deadtime correction and decay correction.

Using the kernel-based image representation leads to the following kernelized forward projection model for dynamic PET reconstruction:

$$\bar{y}_{i,m} = \left(\boldsymbol{PK}\boldsymbol{\alpha}_m + \boldsymbol{s}_m + \boldsymbol{r}_m\right)_i$$

Based on this model, the ML estimate of $\boldsymbol{\alpha}$ can be obtained from the list-mode raw data using the kernelized expectation maximization (KEM) algorithm [31],

$$\hat{\alpha}_{j,m}^{n+1} = \frac{\hat{\alpha}_{j,m}^{n}}{\epsilon_j} \sum_{k=1}^{K} \frac{P_{i_k j}}{\left(\boldsymbol{PK}\boldsymbol{\alpha}_m^n + \boldsymbol{s}_m + \boldsymbol{r}_m\right)_{i_k}}$$

with $\boldsymbol{\alpha}^0$ starting from a uniform image.

The most common way for building the kernel matrix $\boldsymbol{K}$ is by use of composite frames derived from the dynamic data prior to the frame-by-frame reconstruction [31]. For example, a one-hour dynamic ^{18}F-FDG PET scan can be first rebinned into three composite frames, e.g., 10 minutes, 20 minutes and 30 minutes [2]. From the reconstructed composite images $\left\{\boldsymbol{x}_m^{\text{reb}}\right\}_{m=1}^{3}$ (e.g., by standard EM reconstruction), three time-activity points are obtained for the j^{th} voxel and form a feature vector $\boldsymbol{f}_j = \left[x_{j,1}^{\text{reb}}, x_{j,2}^{\text{reb}}, x_{j,3}^{\text{reb}}\right]^T$ The $(j, l)^{th}$ element of the kernel matrix $\boldsymbol{K}$ is then calculated by

$$K_{j,l} = k\left(\boldsymbol{f}_j, \boldsymbol{f}_l\right)$$

where $\kappa(\cdot,\cdot)$ denotes the kernel function. One example is the radial Gaussian kernel function

$$\kappa\left(\boldsymbol{f}_j, \boldsymbol{f}_l\right) = \exp\left(-\left\|\boldsymbol{f}_j - \boldsymbol{f}_l\right\|^2 / 2\sigma^2\right)$$

with σ the kernel parameter, e.g., $\sigma = 1$.

A total-body image has a very large image size (e.g., 256 × 256 × 828; with high count – density, it is possible for images to be larger still). For practical use, $\boldsymbol{K}$ is commonly built to be sparse. This is achieved by restricting the voxel l to be in a neighborhood of the voxel j. A typical example is through the k-nearest neighbor (kNN) search within a 7 × 7 × 7 neighborhood window with k set to be 50.

The KEM reconstruction approach can improve total-body dynamic image significantly as compared to conventional 3D MLEM reconstruction [2]. Figure 11 shows a comparison of standard EM reconstruction and the KEM reconstruction for two short frames. Compared with other potential 4D reconstruction approaches, one big advantage of the KEM algorithm is that the reconstruction of a frame is implemented independently from other frames without any direct temporal interaction from each other during the reconstruction. This is

particularly beneficial in total-body dynamic PET because a fully 4D reconstruction has a much bigger data size to handle and hence is more computationally intensive than frame-by-frame 3D reconstruction. The kernel method can achieve a balance to bring a significant improvement in image quality while maintaining computational efficiency. For further improved performance, temporal correlations can be also incorporated into the kernel framework to form a spatiotemporal kernel method which can be particularly beneficial to high-temporal resolution dynamic PET imaging [34].

4.2 Direct estimation of kinetic parameters

One of the important purposes of dynamic PET imaging is quantification of tracer kinetics. The conventional framework is to first perform dynamic PET reconstruction and then follow with tracer kinetic modeling in a region of interest or at voxel level [35,36]. This "indirect method" may be suboptimal because information loss can occur in the two separate steps. Alternatively, direct estimation of kinetic parameters can be performed by combining the underlying temporal kinetic model and the reconstruction into a single formula, which has the potential to better exploit the available dynamic data [37–40].

The forward projection model for direct reconstruction can be formulated as

$$\bar{y}_{i,m} = \left[\boldsymbol{P}\boldsymbol{x}_m(\boldsymbol{\theta}) + \boldsymbol{s}_m + \boldsymbol{r}_m\right]_i$$

where the dynamic image of the m^{th} frame, $\boldsymbol{x}_m$, is explicitly expressed as a function of the kinetic parametric images $\boldsymbol{\theta}$,

$$x_m\left(\boldsymbol{\theta}_j\right) = \int_{t_{m,s}}^{t_{m,e}} C_T\left(\tau;\boldsymbol{\theta}_j\right) e^{-\lambda\tau} d\tau$$

where $t_{m,s}$ and $t_{m,e}$ are the start and end times of time frame m, and λ is the decay constant of the radiotracer. $C_T(t;\boldsymbol{\theta}_j)$ is the tracer concentration in voxel j at time t and is determined by a linear or nonlinear model with the kinetic parameter vector $\boldsymbol{\theta}_j$. Examples include B-splines, spectral analysis, Patlak model, one-tissue compartmental model, irreversible and reversible two-tissue compartmental models. [37,41]

One major challenge for direct reconstruction, in particular for total-body dynamic PET, is the optimization algorithm becomes very complicated and not trivial to implement because the 4D dataset is spatiotemporally coupled. This challenge can be overcome by using the optimization transfer methods [40,42]. The optimization transfer method with the separable paraboloidal (SP) surrogate function [40] can transfer the 4D reconstruction problem into a voxel-wise 1D nonlinear least-square fitting problem at each voxel j as defined by

$$\hat{\boldsymbol{\theta}}_j^{n+1} = \underset{\boldsymbol{\theta}_j}{\operatorname{argmin}} \sum_{m=1}^{N_m} \widehat{W}_{j,m}^n \left[\hat{x}_{j,m}^n - x_m\left(\boldsymbol{\theta}_j\right)\right]^2$$

where $\left\{\hat{x}_{j,m}^{n}\right\}_{m=1}^{N_m}$ denotes the intermediate time activity curve (TAC) estimated from the projection data for the j^{th} voxel based on the SP surrogate at reconstruction iteration n. $\widehat{W}_{j,m}^{n}$ are the corresponding weights resulting from the optimization transfer [40]. $x_m\left(\boldsymbol{\theta}_j\right)$ represents the model TAC based on the kinetic parameter set $\boldsymbol{\theta}_j$. This 1D fitting problem can be easily solved by many existing optimization algorithms (e.g. the Levenberg-Marquardt algorithm) in tracer kinetic modeling.

Alternatively, the optimization transfer method with the EM surrogate function [42] can also transfer the 4D reconstruction into the following equivalent voxel-wise Poisson likelihood-like 1D fitting problem:

$$\hat{\boldsymbol{\theta}}_j^{n+1} = \underset{\boldsymbol{\theta}_j}{\operatorname{argmax}} \sum_{m=1}^{N_m} \hat{x}_{j,m}^{n} \ln x_m\left(\boldsymbol{\theta}_j\right) - x_m\left(\boldsymbol{\theta}_j\right)$$

where $\hat{\boldsymbol{x}}_j^n \triangleq \left\{\hat{x}_{j,m}^{n}\right\}_{m=1}^{N_m}$ now represents the intermediate TAC estimated from the project data using one-iteration of the standard EM reconstruction update. Such 1D fitting can be also solved by different fitting algorithms, including the popular Levenberg-Marquardt algorithm.

One special case of the EM-based optimization transfer method is the Nested EM algorithm [43] developed for linear kinetic models. Assume a linear kinetic model,

$$x_m\left(\boldsymbol{\theta}_j\right) = \left(\boldsymbol{B}\boldsymbol{\theta}_j\right)_m,$$

where $\boldsymbol{B}$ denotes the temporal basis matrix following a specific kinetic model. Then the estimation of $\boldsymbol{\theta}_j$ can be obtained from the intermediate TAC $\hat{\boldsymbol{x}}_j^n$, using the following EM update with N_q sub iterations [43],

$$\hat{\boldsymbol{\theta}}_j^{n,q+1} = \frac{\hat{\boldsymbol{\theta}}_j^{q}}{\boldsymbol{B}^T\mathbf{1}} \cdot \left[\boldsymbol{B}^T \frac{\hat{\boldsymbol{x}}_j^n}{\left(\boldsymbol{B}\boldsymbol{\theta}_j^{n,q}\right)_m}\right], \quad \mathrm{q}=0,\cdots,\mathrm{N}_q-1$$

where the vector division is operated element-wise. $\hat{\boldsymbol{\theta}}_j^{n+1}$ is finally obtained as $\hat{\boldsymbol{\theta}}_j^{n+1} = \hat{\boldsymbol{\theta}}_j^{n,N_q}$.

Figure 12 shows the application of the direct estimation to parametric imaging of the slope (reflecting FDG influx rate) of the Patlak plot for a dynamic ^{18}F-FDG PET scan on the uEXPLORER scanner. As compared to the conventional indirect method, the direct reconstruction demonstrated substantial noise suppression. More quantitative comparisons can be found in the recent work of Zhang *et al.* [2].

5. Summary and future prospects

Total-body PET provides both challenges and opportunities for 3D/4D PET image reconstruction. On the one hand, the large dataset size presents a daunting challenge in computation. Incorporation of the long oblique LORs in reconstruction also requires an accurate model of the response function and proper handling of the correction factors, such as normalization and scatter correction. On the other hand, the high photon-detection sensitivity of total-body PET provides sufficient count density to take advantage of more sophisticated resolution models. Examples include modeling of positron range and photon acollinearity, two factors that put a fundamental limit on PET spatial resolution. While methods for modeling these two effects have been studied before[44–46], standard scans on existing whole-body PET scanners are too noisy to exploit these models to enhance the spatial resolution of PET. Total-body PET brings the opportunities to utilize these models to push the PET resolution beyond these limits. Another opportunity is the combination of total-body PET with machine learning techniques. While direct reconstruction by neural network[47] for total-body PET may not be feasible with current computing hardware, machine learning can be used to improve the image quality and/or reduce radiation dose[47–56]. For example, combining the kernel reconstruction with the EXPLORER scanner, researchers have obtained high-quality blood flow images at 100-ms temporal resolution[57]. With the help of deep neural network, it may be possible to generate motion-freeze total-body PET images under a single breath hold. As more total-body PET scanners become operational, we expect to see many new advances in total-body PET image reconstruction.

Acknowledgments

Dr. Qi reports support by grants from the National Institute of Biomedical Imaging and Bioengineering (NIBIB) and the National Cancer Institute (NCI) of the National Institutes of Health (NIH) under Award Nos. R01EB000194, R21EB026668, R01CA206187 and funding through a sponsored research agreement by Canon Medical Research USA.

Dr. Wang reports support by grants from NCI and NIBIB under Award Nos. K12 CA138464, R01CA206187, P30CA093373, and R21 EB027346.

Dr. Matej reports support by grants from the National Institute of Biomedical Imaging and Bioengineering and the National Cancer Institute of the National Institutes of Health under Award Nos. R01EB023274, R01CA113941, R01CA196528, and R33CA225310 and funding through a sponsored research agreement by Siemens Medical Solutions USA. Dr. Matej serves also as a consultant for Siemens Medical Solutions USA.

7. References

1. Badawi RD, Shi H, Hu P, et al. First Human Imaging Studies with the EXPLORER Total-Body PET Scanner. J Nucl Med. 2019;60(3):299–303. [PubMed: 30733314]
2. Zhang X, Xie Z, Berg E, et al. Total-Body Dynamic Reconstruction and Parametric Imaging on the uEXPLORER. J Nucl Med. 2020;61(2):285–291. [PubMed: 31302637]
3. Huesman RH, Klein GJ, Moses WW, Qi J, Reutter BW, Virador PR. List-mode maximum-likelihood reconstruction applied to positron emission mammography (PEM) with irregular sampling. IEEE transactions on medical imaging. 2000;19(5):532–537. [PubMed: 11021696]
4. Parra L, Barrett HH. List-mode likelihood: EM algorithm and image quality estimation demonstrated on 2-D PET. IEEE Trans Med Imaging. 1998;17(2):228–235. [PubMed: 9688154]
5. Barrett HH, White T, Parra LC. List-mode likelihood. J Opt Soc Am A Opt Image Sci Vis. 1997;14(11):2914–2923. [PubMed: 9379247]

6. Qi J, Leahy RM. Iterative reconstruction techniques in emission computed tomography. Physics in Medicine & Biology. 2006;51(15):R541. [PubMed: 16861768]
7. Tohme MS, Qi J. Iterative image reconstruction for positron emission tomography based on a detector response function estimated from point source measurements. Physics in medicine & biology. 2009;54(12):3709. [PubMed: 19478379]
8. Gong K, Zhou J, Tohme M, Judenhofer M, Yang Y, Qi J. Sinogram blurring matrix estimation from point sources measurements with rank-one approximation for fully 3-D PET. IEEE transactions on medical imaging. 2017;36(10):2179–2188. [PubMed: 28613163]
9. Zhou J, Qi J. Fast and efficient fully 3D PET image reconstruction using sparse system matrix factorization with GPU acceleration. Physics in Medicine & Biology. 2011;56(20):6739. [PubMed: 21970864]
10. Zhou J, Qi J. Efficient fully 3D list-mode TOF PET image reconstruction using a factorized system matrix with an image domain resolution model. Physics in Medicine & Biology. 2014;59(3):541. [PubMed: 24434568]
11. Carney JP, Townsend DW, Rappoport V, Bendriem B. Method for transforming CT images for attenuation correction in PET/CT imaging. Med Phys. 2006;33(4):976–983. [PubMed: 16696474]
12. Kinahan PE, Hasegawa BH, Beyer T. X-ray-based attenuation correction for positron emission tomography/computed tomography scanners. Semin Nucl Med. 2003;33(3):166–179. [PubMed: 12931319]
13. Oliver JF, Rafecas M. Modelling Random Coincidences in Positron Emission Tomography by Using Singles and Prompts: A Comparison Study. PLoS One. 2016;11(9):e0162096. [PubMed: 27603143]
14. Oliver JF, Rafecas M. Improving the singles rate method for modeling accidental coincidences in high-resolution PET. Phys Med Biol. 2010;55(22):6951–6971. [PubMed: 21048288]
15. Brasse D, Kinahan PE, Lartizien C, Comtat C, Casey M, Michel C. Correction methods for random coincidences in fully 3D whole-body PET: impact on data and image quality. J Nucl Med. 2005;46(5):859–867. [PubMed: 15872361]
16. Schmall JP, Karp JS, Werner M, Surti S. Parallax error in long-axial field-of-view PET scanners-a simulation study. Physics in medicine and biology. 2016;61(14):5443–5455. [PubMed: 27367971]
17. Zhang X, Zhou J, Cherry SR, Badawi RD, Qi J. Quantitative image reconstruction for total-body PET imaging using the 2-meter long EXPLORER scanner. Phys Med Biol. 2017;62(6):2465–2485. [PubMed: 28240215]
18. Badawi RD, Marsden PK. Developments in component-based normalization for 3D PET. Phys Med Biol. 1999;44(2):571–594. [PubMed: 10070802]
19. Bai B, Li Q, Holdsworth CH, et al. Model-based normalization for iterative 3D PET image reconstruction. Phys Med Biol. 2002;47(15):2773–2784. [PubMed: 12200938]
20. Poon JK, Dahlbom ML, Moses WW, et al. Optimal whole-body PET scanner configurations for different volumes of LSO scintillator: a simulation study. Phys Med Biol. 2012;57(13):4077–4094. [PubMed: 22678106]
21. Karp JS, Viswanath V, Geagan MJ, et al. PennPET Explorer: Design and Preliminary Performance of a Whole-Body Imager. J Nucl Med. 2020;61(1):136–143. [PubMed: 31227573]
22. Matej S, Surti S, Jayanthi S, Daube-Witherspoon ME, Lewitt RM, Karp JS. Efficient 3-D TOF PET reconstruction using view-grouped histo-images: DIRECT - Direct Image Reconstruction for TOF. IEEE Trans Med Imaging. 2009;28(5):739–751. [PubMed: 19150784]
23. Politte DG, Hoffman GR, Beecher DE, Ficke DC, Holmes TJ, Ter-Pogosian MM. Image-reconstruction of data from super PETT I: A first-generation time-of-flight positron-emission tomograph (Reconstruction from reduced-angle data). IEEE Trans Nucl Sci. 1986;33(1):428–434.
24. Vandenberghe S, Daube-Witherspoon ME, Lewitt RM, Karp JS. Fast reconstruction of 3D time-of-flight PET data by axial rebinning and transverse mashing. Phys Med Biol. 2006;51(6): 1603–1621. [PubMed: 16510966]
25. Ha S, Matej S, Ispiryan M, Mueller K. GPU-accelerated forward and back-projection with spatially varying kernels in 3D DIRECT TOF PET reconstruction. IEEE Trans Nucl Sci. 2013;60(1):166–173. [PubMed: 23531763]

26. Daube-Witherspoon ME, Matej S, Werner ME, Surti S, Karp JS. Comparison of list-mode and DIRECT approaches for time-of-flight PET reconstruction. IEEE Trans Med Imaging. 2012;31(7): 1461–1471. [PubMed: 22410326]
27. Matej S, Kazantsev IG. Fourier-based reconstruction for fully 3-D PET: optimization of interpolation parameters. IEEE Trans Med Imaging. 2006;25(7):845–854. [PubMed: 16827486]
28. Kinahan PE, Rogers JG. Analytic 3D image reconstruction using all detected events. IEEE Trans Nucl Sci. 1989;36:964–968.
29. Matej S, Lewitt RM. 3D-FRP: Direct Fourier reconstruction with Fourier reprojection for fully 3-D PET. IEEE Trans Nucl Sci. 2001;48(4):1378–1385.
30. Matej S, Daube-Witherspoon ME, Karp JS. Analytic TOF PET reconstruction algorithm within DIRECT data partitioning framework. Phys Med Biol. 2016;61(9):3365–3386. [PubMed: 27032968]
31. Wang G, Qi J. PET image reconstruction using kernel method. IEEE Transactions on Medical Imaging. 2015;34(1):61–71. [PubMed: 25095249]
32. Hutchcroft W, Wang G, Chen KT, Catana C, Qi J. Anatomically-aided PET reconstruction using the kernel method. Physics in medicine and biology. 2016;61(18):6668–6683. [PubMed: 27541810]
33. Gong K, Cheng-Liao JX, Wang GB, Chen KT, Catana C, Qi JY. Direct Patlak Reconstruction From Dynamic PET Data Using the Kernel Method With MRI Information Based on Structural Similarity. IEEE Transactions on Medical Imaging. 2018;37(4):955–965. [PubMed: 29610074]
34. Wang GB. High temporal-resolution dynamic PET image reconstruction using a new spatiotemporal kernel method. IEEE Transactions on Medical Imaging. 2019;38(3):664 – 674. [PubMed: 30222553]
35. Rahmim A, Tang J, Zaidi H. Four-dimensional (4D) image reconstruction strategies in dynamic PET: Beyond conventional independent frame reconstruction. Medical Physics. 2009;36(8):3654–3670. [PubMed: 19746799]
36. Reader AJ, Verhaeghe J. 4D image reconstruction for emission tomography. Physics in Medicine and Biology. 2014;59(22):R371–R418. [PubMed: 25361380]
37. Wang G, Qi J. Direct estimation of kinetic parametric images for dynamic PET. Theranostics. 2013;3(10):802–815. [PubMed: 24396500]
38. Kamasak ME, Bouman CA, Morris ED, Sauer K. Direct reconstruction of kinetic parameter images from dynamic PET data. IEEE Transactions on Medical Imaging. 2005;24(5):636–650. [PubMed: 15889551]
39. Wang G, Fu L, Qi J. Maximum a posteriori reconstruction of the Patlak parametric image from sinograms in dynamic PET. Physics in Medicine and Biology. 2008;53(3):593–604. [PubMed: 18199904]
40. Wang G, Qi J. Generalized Algorithms for Direct Reconstruction of Parametric Images From Dynamic PET Data. IEEE Transactions on Medical Imaging. 2009;28(11):1717–1726. [PubMed: 19447699]
41. Carson RE. Tracer Kinetic Modeling in PET. In: Bailey DL, Townsend DW, Valk PE, Maisey MN, eds. Positron Emission Tomography. London: Springer; 2005.
42. Wang G, Qi J. Penalized Likelihood PET Image Reconstruction Using Patch-Based Edge-Preserving Regularization. IEEE Transactions on Medical Imaging. 2012;31(12):2194–2204. [PubMed: 22875244]
43. Wang G, Qi J. Acceleration of the direct reconstruction of linear parametric images using nested algorithms. Physics in Medicine and Biology. 2010;55(5):1505–1517. [PubMed: 20157226]
44. Bertolli O, Eleftheriou A, Cecchetti M, Camarlinghi N, Belcari N, Tsoumpas C. PET iterative reconstruction incorporating an efficient positron range correction method. Phys Med. 2016;32(2): 323–330. [PubMed: 26818471]
45. Fu L, Qi J. A residual correction method for high-resolution PET reconstruction with application to on-the-fly Monte Carlo based model of positron range. Med Phys. 2010;37(2):704–713. [PubMed: 20229880]
46. Alessio A, MacDonald L. Spatially Variant Positron Range Modeling Derived from CT for PET Image Reconstruction. IEEE Nucl Sci Symp Conf Rec (1997). 2008;2008:3637–3640.

47. Haggstrom I, Schmidtlein CR, Campanella G, Fuchs TJ. DeepPET: A deep encoder-decoder network for directly solving the PET image reconstruction inverse problem. Med Image Anal. 2019;54:253–262. [PubMed: 30954852]

48. Ouyang J, Chen KT, Gong E, Pauly J, Zaharchuk G. Ultra-low-dose PET reconstruction using generative adversarial network with feature matching and task-specific perceptual loss. Med Phys. 2019;46(8):3555–3564. [PubMed: 31131901]

49. Liu CC, Qi J. Higher SNR PET image prediction using a deep learning model and MRI image. Phys Med Biol. 2019;64(11):115004. [PubMed: 30844784]

50. Kim K, Wu D, Gong K, et al. Penalized PET Reconstruction Using Deep Learning Prior and Local Linear Fitting. IEEE Trans Med Imaging. 2018;37(6):1478–1487. [PubMed: 29870375]

51. Gong K, Guan J, Liu C-C, Qi J. PET image denoising using a deep neural network through fine tuning. IEEE Transactions on Radiation and Plasma Medical Sciences. 2018;3(2): 153–161. [PubMed: 32754674]

52. Gong K, Guan J, Kim K, et al. Iterative PET image reconstruction using convolutional neural network representation. IEEE transactions on medical imaging. 2018;38(3):675–685. [PubMed: 30222554]

53. Gong K, Catana C, Qi J, Li Q. PET Image Reconstruction Using Deep Image Prior. IEEE transactions on medical imaging. 2018.

54. Xiang L, Qiao Y, Nie D, An L, Wang Q, Shen D. Deep Auto-context Convolutional Neural Networks for Standard-Dose PET Image Estimation from Low-Dose PET/MRI. Neurocomputing. 2017;267:406–416. [PubMed: 29217875]

55. Xie Z, Baikejiang R, Li T, et al. Generative adversarial network based regularized image reconstruction for PET. Phys Med Biol. 2020;65(12):125016. [PubMed: 32357352]

56. Gong K, Berg E, Cherry SR, Qi J. Machine Learning in PET: From Photon Detection to Quantitative Image Reconstruction. Proceedings of the IEEE. 2020;108(1):51–68.

57. Zhang X, Cherry SR, Xie Z, Shi H, Badawi RD, Qi J. Subsecond total-body imaging using ultrasensitive positron emission tomography. Proc Natl Acad Sci U S A. 2020;117(5):2265–2267. [PubMed: 31964808]

Key Points

- Long axial FOV data bring new imaging opportunities and potentials of improved reconstruction quality, but also challenges dues to dramatic increase of data sizes and challenges given by the change and variations of data characteristics with increased acceptance angles
- Good TOF resolution and considerably increased sensitivity of total-body imaging scanners allow novel and improved modeling and ways of processing their data
- Total-body PET enables simultaneous dynamic imaging of the entire body. 4D reconstruction using the kernel method and/or direct estimation of kinetic parameters can further improve image quality for total-body parametric imaging

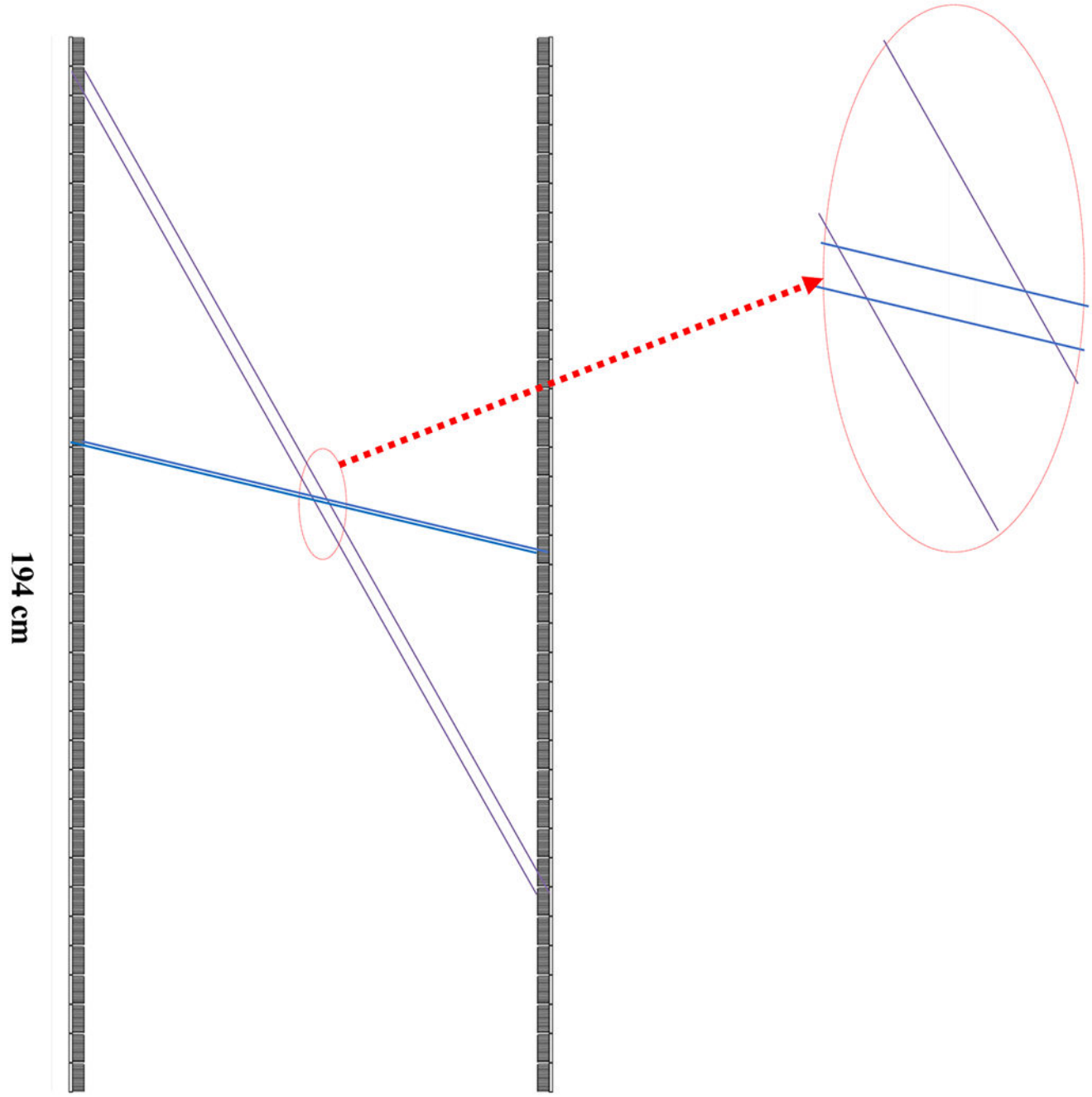

Figure 1.
Illustration of the difference in axial resolution between an LOR with a small ring difference (blue) and an LOR with a large ring difference (purple).

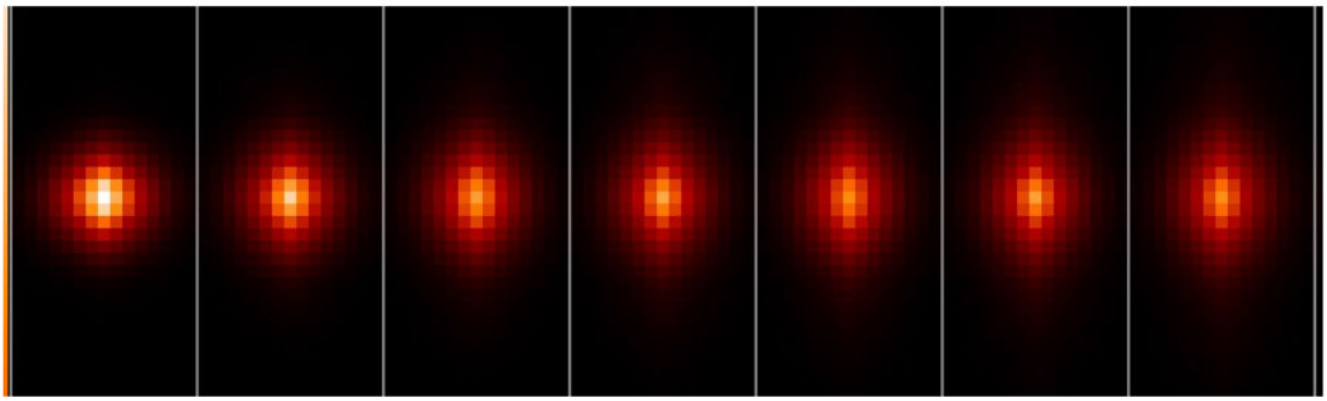

Figure 2.
Sagittal slices of reconstructed point source images on the center axis at different axial positions: (left to right) 13 cm, 26 cm, 39 cm, 52 cm, 65 cm, 78 cm, and 91 cm, from the axial edge of the scanner. Vertical axis is the axial direction and horizontal axis is the radial direction.

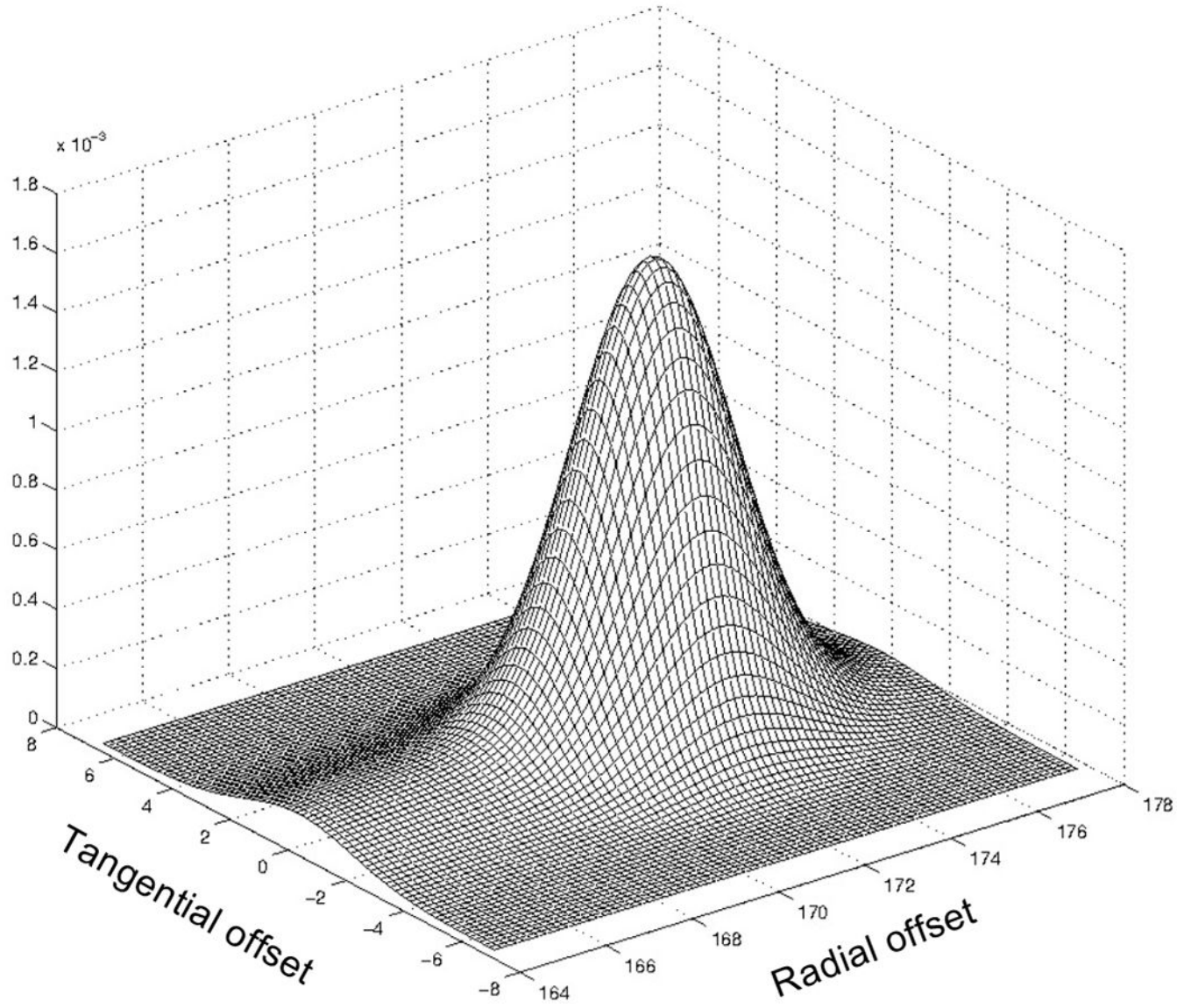

Figure 3.

The transaxial profile of a reconstructed point source at a radial offset of 17.2 cm from the center.

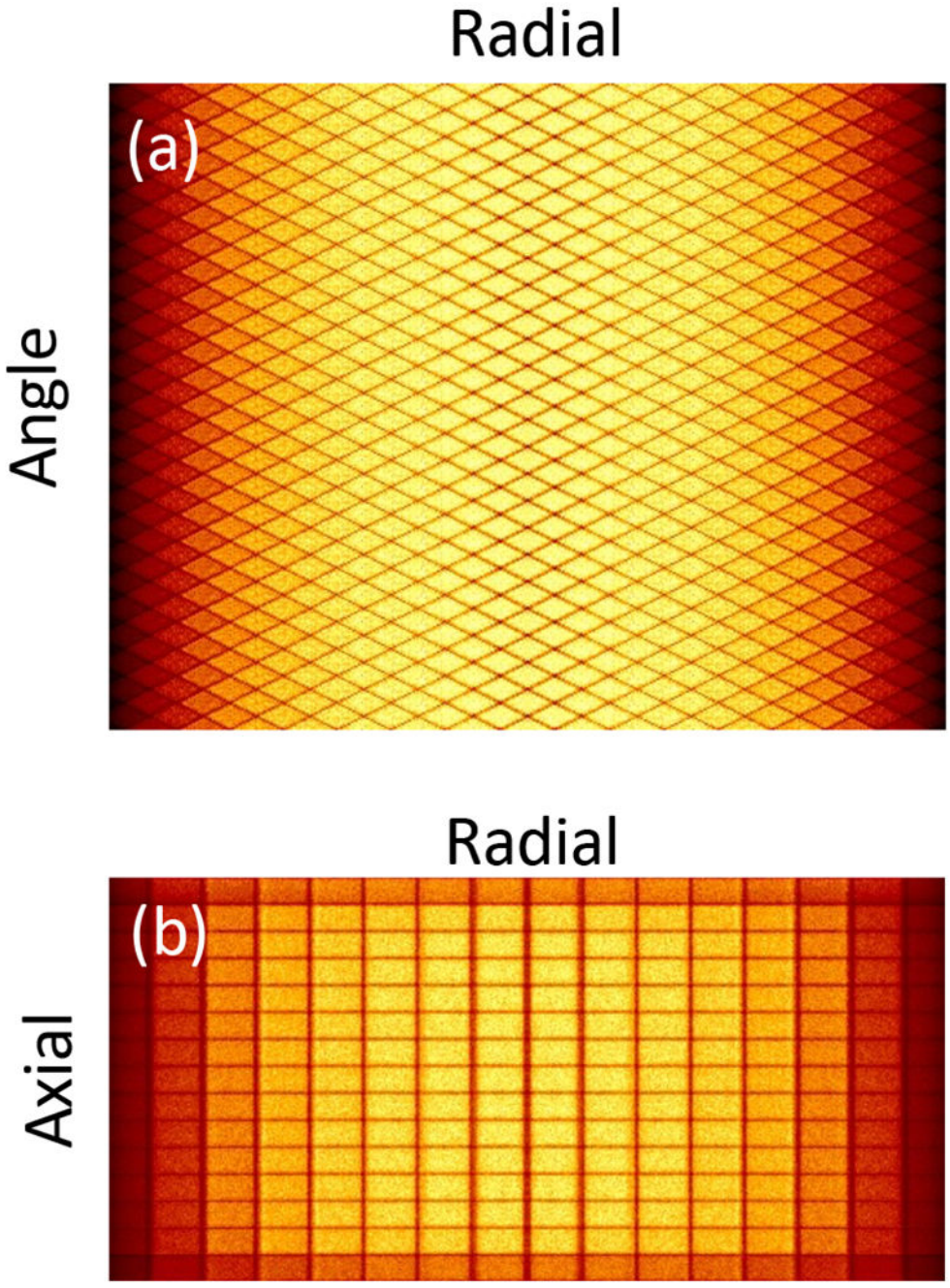

Figure 4.
Sinogram of a uniform cylinder for normalization factor estimation. (a) transaxial view; (b) axial view. Gaps between detector blocks are skipped and only valid LORs shown.

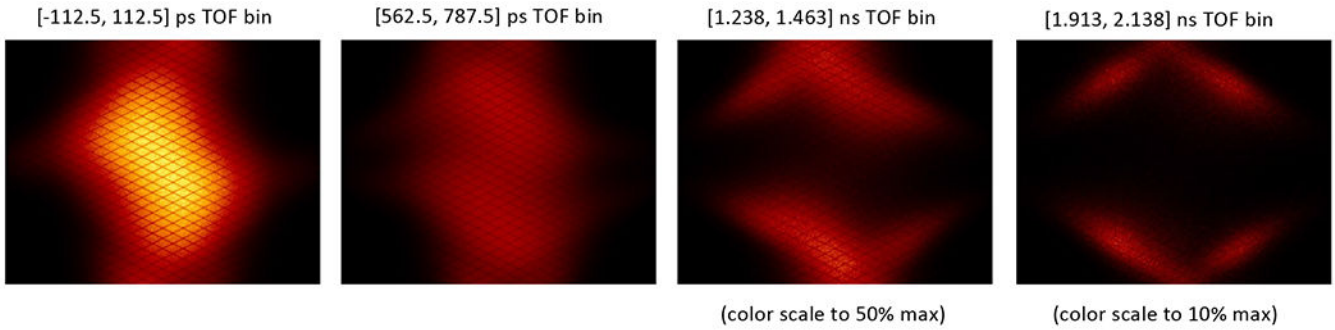

Figure 5.
Estimated scatter Mean Sinogram in four selected TOF Bins.

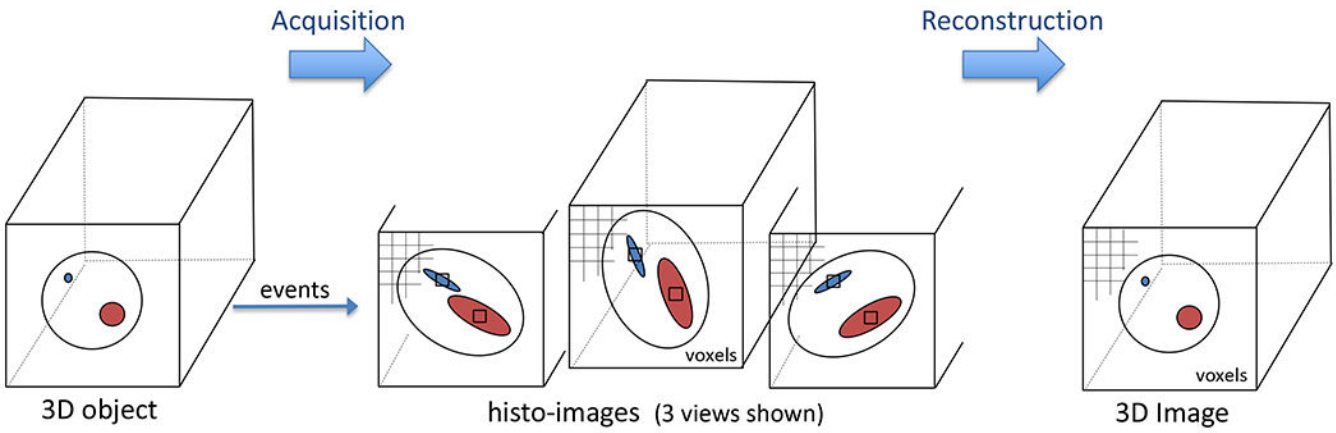

Figure 6.

Illustration of the hist-image partitioning; acquired data are histogrammed into the (most-likely) histo-image voxels having 1-to-1 correspondence with the reconstructed image voxels.

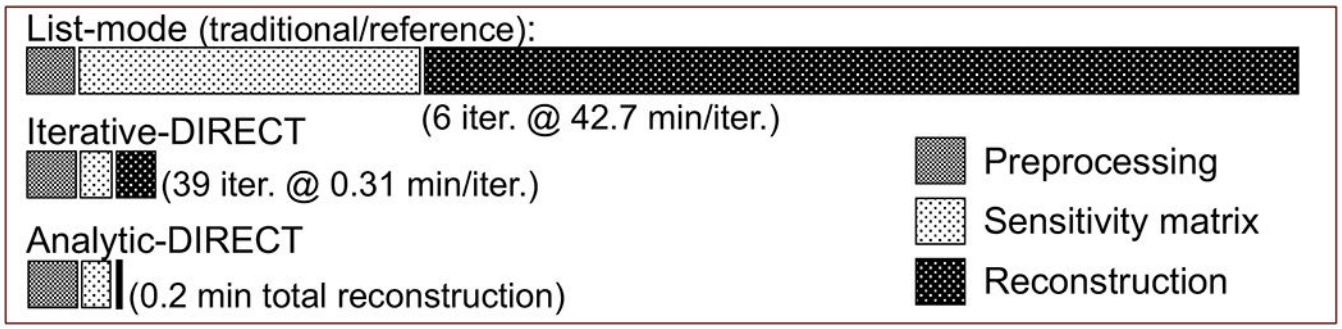

Figure 7.

Relative comparison of processing times for iterative- and analytic-DIRECT to traditional list-mode TOF reconstructions at comparable image quality; times are shown for a single CPU reconstruction of one bed position of a typical patient scan.

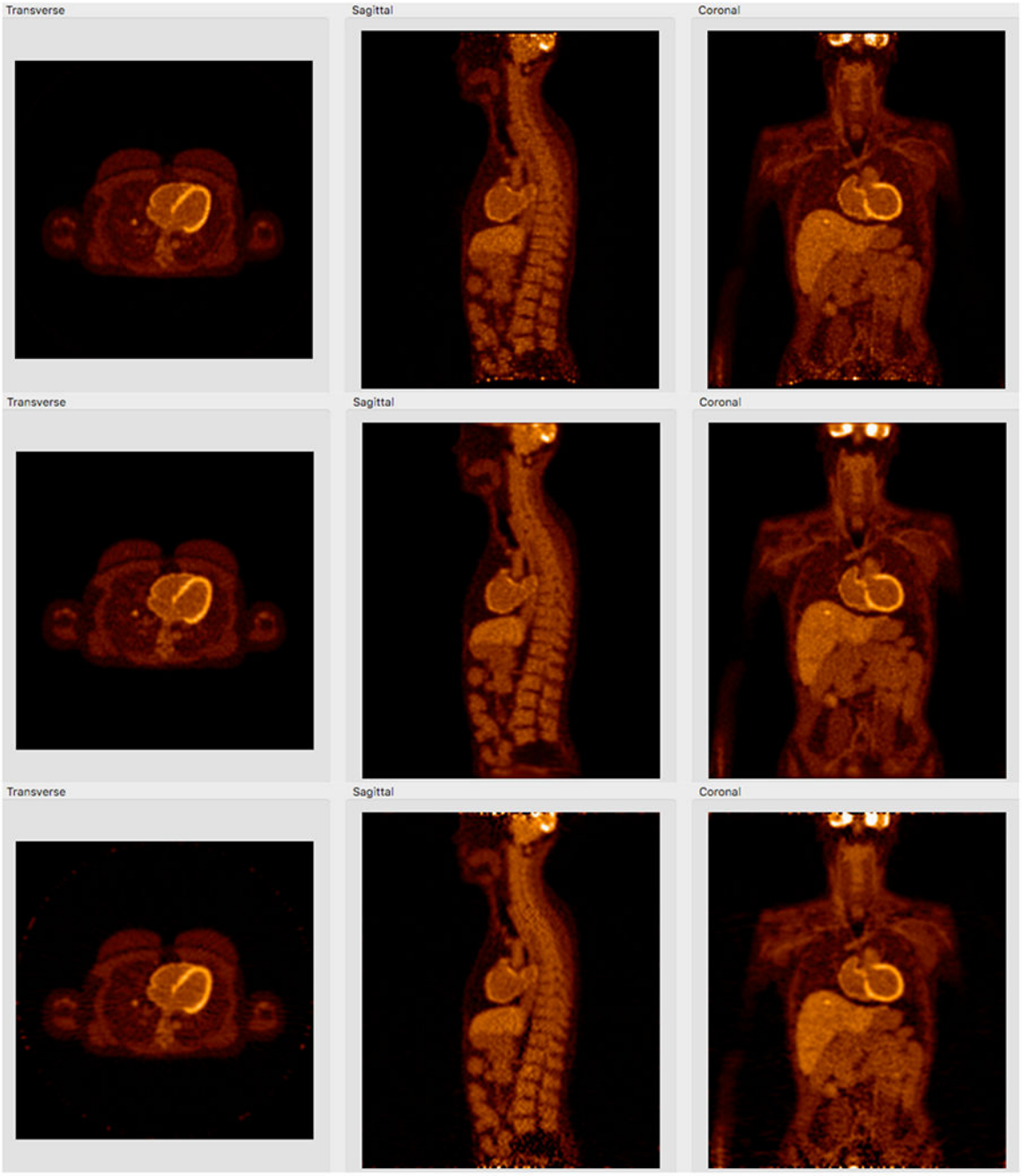

Figure 8.

Comparison of list-mode reconstruction (default tool on PennPET Explorer scanner), iterative-DIRECT (RAMLA), and analytic-DIRECT reconstructions of simulated XCAT phantom data for 70cm PennPET Explorer scanner.

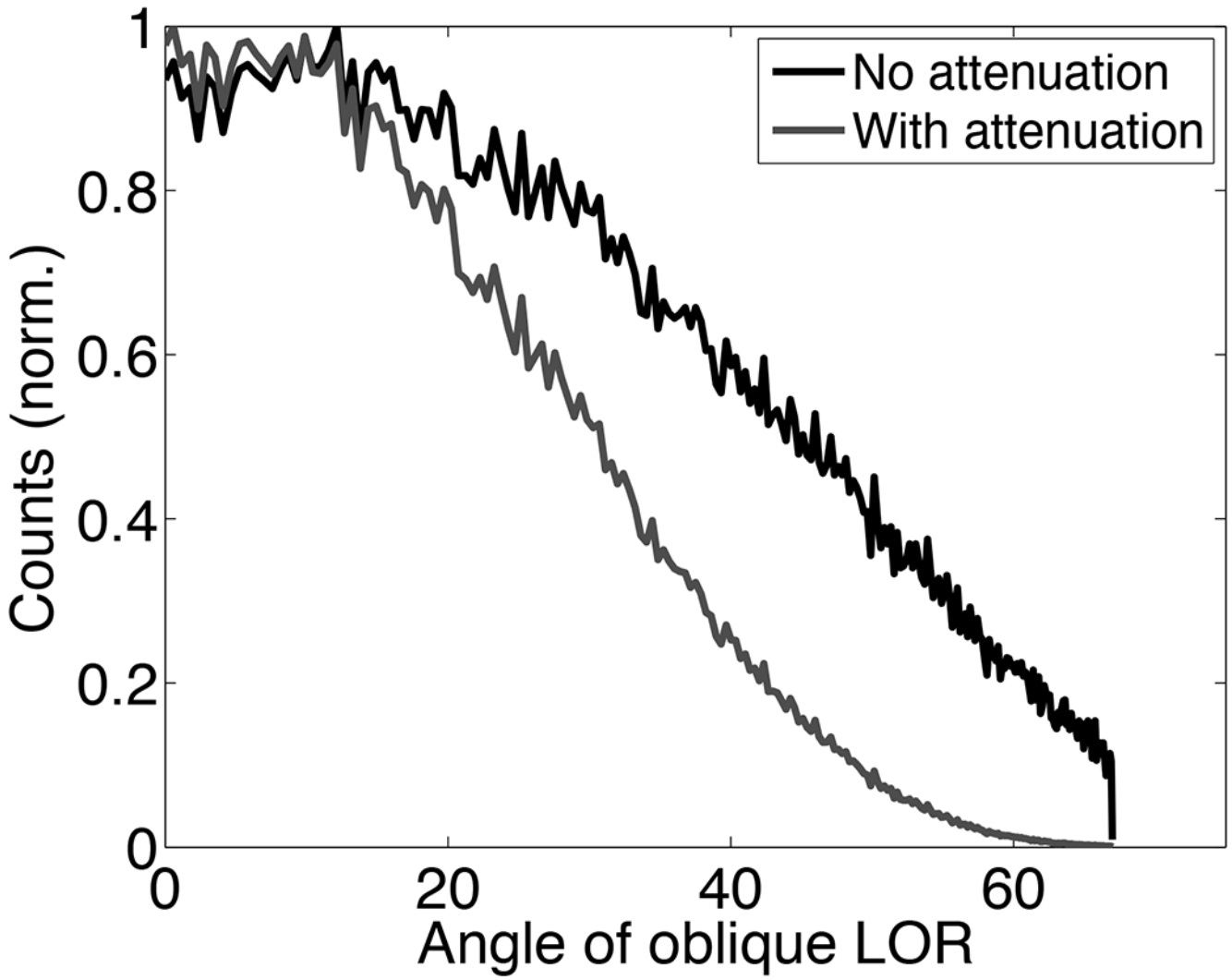

Figure 9.

Recorded coincidence events for a single row of crystals along the axial extent of the simulated scanner 198cm long (plotted as a function of the LOR oblique angle). Results are shown for a single point source at the center of the imaging FOV with and without attenuation of water filled cylinder, 30 cm in diameter and 2 m long. The counts are normalized to the angular bin with the largest number of counts. (From [Jeffrey P Schmall et al 2016 Phys. Med. Biol. 61 5443] [16] © *Institute of Physics and Engineering in Medicine. Reproduced by permission of IOP Publishing. All rights reserved.*)

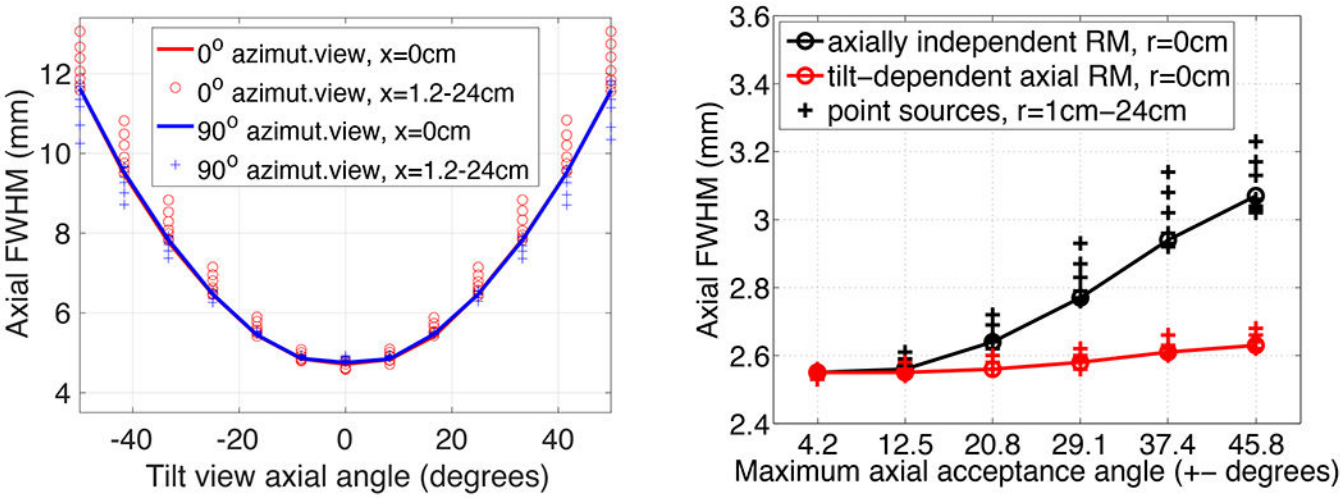

Figure 10.

Axial resolutions of the simulated point-sources for long axial FOV scanner in data and reconstruction spaces. **Left:** Axial FWHMs of PSFs in the histo-image data as a function of oblique angle, **Right:** Axial FWHMs of the point-sources reconstructed with (red) and without (black) axial tilt-dependent resolution models for gradually increasing maximum acceptance angle of used data.

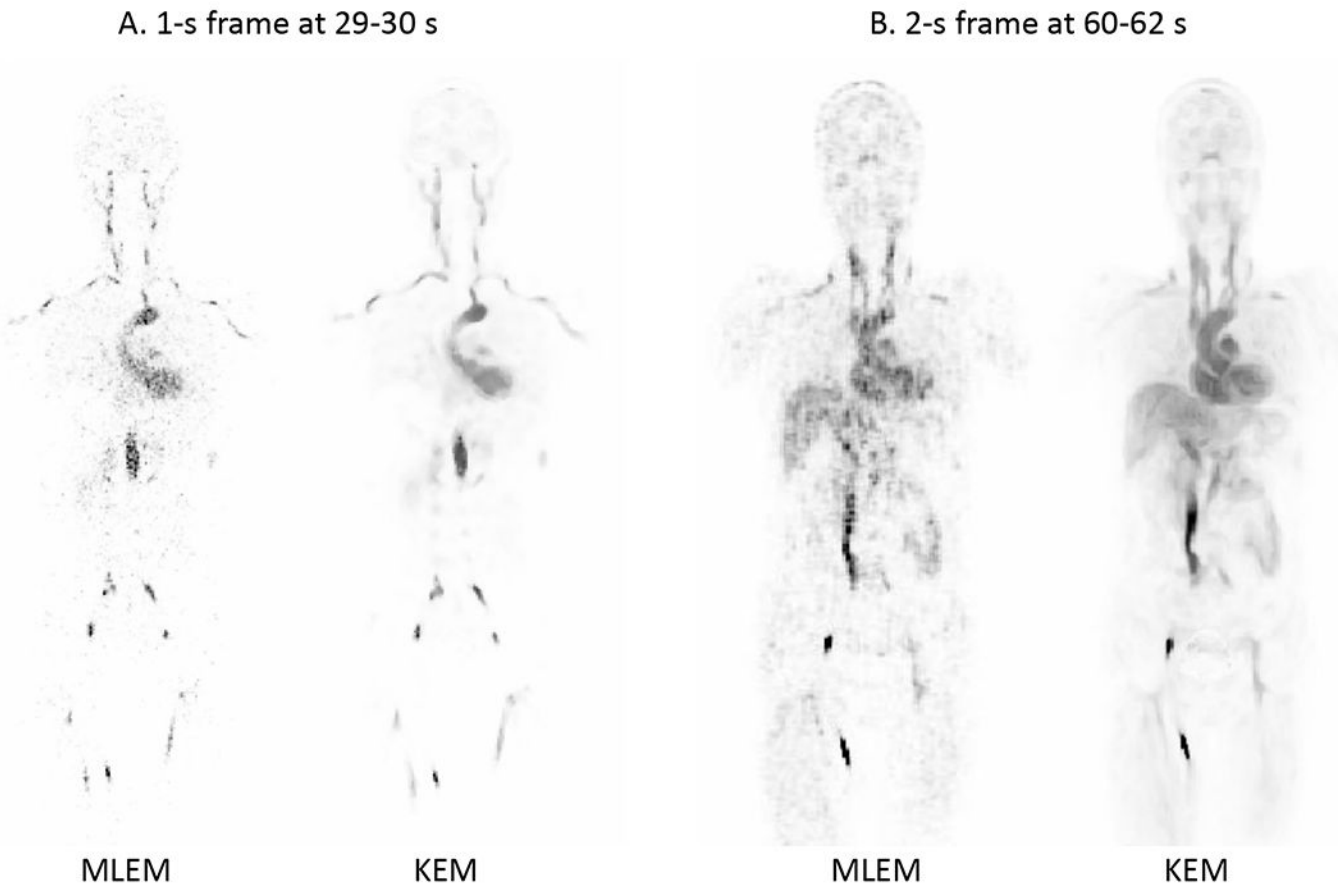

Figure 11.

Comparison of standard maximum-likelihood (ML) expectation-maximization (EM) reconstruction with kernelized EM (KEM) reconstruction for (A) a 1-s frame at 29-30 s post injection and (B) a 2-s frame at 60-62 s post injection. The dynamic data were acquired with ^{18}F-FDG for a human subject on the uEXPLORER total-body PET/CT scanner.

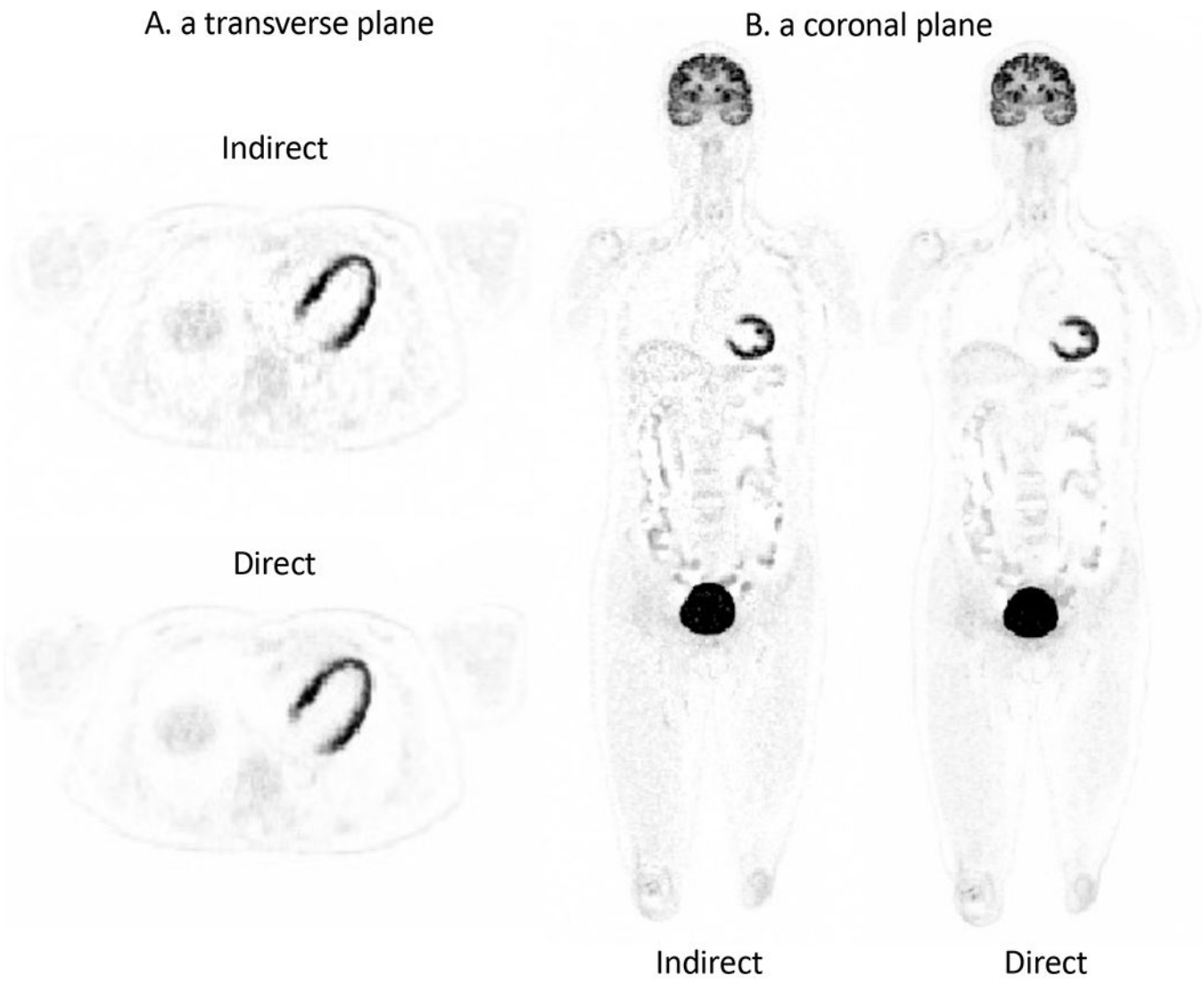

Figure 12:
Comparison of the direct method and indirect method for parametric imaging of the slope of the Patlak plot for a human subject ^{18}F-FDG scan on the uEXPLORER scanner. (A) a transverse plane; (B) a coronal plane.

Table 1.

Radial FWHM and FWTM of the point spread function at various radial positions of a simulated 2-m long EXPLORER (data from [17]).

Radial Offset	0 cm	10 cm	20 cm	30 cm
Radial FWHM	3.0 mm	3.9 mm	5.6 mm	6.8 mm
Radial FWTM	5.4 mm	7.1 mm	10.2 mm	12.3 mm